Optics & Laser Technology 179 (2024) 111281

Contents lists available at ScienceDirect

Optics and Laser Technology

journal homepage: www.elsevier.com/locate/optlastec

Full length article

Flexible wearable optical microfiber sensor for identifying bending direction and body temperature

Wenwen Wang [a], Li Jin [a], Guoxin Shi [a], Ze Xu [a], Yingkuan Guo [a], Bowen Yang [a], Yukun Yang [b], Jizhou Wu [a,c], Dandan Sun [a,*], Jie Ma [a,c,*]

[a] School of Physics and Electronic Engineering, Shanxi University, Taiyuan 030006, China
[b] School of Life Science, Shanxi University, Taiyuan 030006, China
[c] Collaborative Innovation Center of Extreme Optics, Shanxi University, Taiyuan 030006, China

ARTICLE INFO

Keywords:
Wearable
Bending direction
Body temperature
Multi-parameter monitoring
Bio-health monitoring

ABSTRACT

A flexible wearable optical microfiber sensor for identifying bending direction and body temperature is proposed and demonstrated. The sensor is composed of microfiber as the core sensing node and a double layer of different membranes of molybdenum disulfide (MoS_2) and (PDMS) as the sensor encapsulation. Due to the strain amplification effect of the microfiber, the sensor's sensitivity to bending curvature and temperature is significantly improved, and it can achieve real-time monitoring of the obverse and reverse bending curvature of the wrist and human body temperature, In the curvature range of 4.31 to 6.10 m^{-1}, the sensitivity responses for reverse bending and obverse bending are 23.62 nm/m^{-1} and 2.70 nm/m^{-1}, respectively, and the temperature sensitivity is about 1.10 nm/°C for the range of 35 to 42 °C. The wrist bending experiment based on the sensor is successful, which proves the high sensitivity and stability of the sensor for the bending direction detection. In addition, the success of the temperature experiment of the sensor also fully proves the feasibility of detecting body temperature. In order to overcome the cross-sensitivity of temperature, a sensitivity matrix is established to realize simultaneous demodulation with two parameters. The proposed wearable sensor provides a new optical alternative for future multi-parameter monitoring, which is crucial for next-generation advances in bio-health monitoring and rehabilitation training.

1. Introduction

Wearable sensors in today's society offer multiple benefits, which provide users with more physiological, movement and environmental data, as well as a smarter and more personalised experience Trung and Lee (2016), [1–5]. Wearable devices demand more miniaturisation and flexibility from sensors in addition to superior sensing capabilities. The selection and packaging of flexible materials and devices has become critical for wearable sensor manufacturing. The flexible wearable sensor can measure various physical parameters such as obverse and reverse bending curvature and temperature. The wrist is one of the most active parts of human tissue and the wrist is more susceptible to injuries that can lead to dysfunction. Loss of wrist mobility can be secondary to muscle weakness, deformity, swelling, and pain, Therefore, the detection of the wrist is very important [6]. Today, flexible electronic sensors are taking the absolute lead in the wearable device market. A number of conductive nanomaterials and polymers such as graphene nanotubes, carbon nanotubes [15,7,8], and other composites have been combined with electronic sensors [9–11], but the electronic metal components are less biocompatible and harmful to the body when worn for a long period of time, and they may suffer from electromagnetic interference and have leakage hazards, which hinders their application in some complex and demanding environments. Therefore, the development of a sensor with advantage of highly biocompatible and not subject to the hazards of electromagnetic interference and leakage is of great significance and a great challenge.

The emergence of photonic sensor provides a new option. Especially in recent years, fiber-optic sensors with broadband, long-distance transmission and multi-parameter functions have a series of unique advantages such as corrosion resistance and anti-electromagnetic interference, which make them have a broad application prospect [11]. At present, fiber optic wearable sensors are widely used in many types of monitoring such as temperature [12,13], bending [14–16], strain [17,23], biosensing [19–21], and so on. In 2017, Yanping Li et al.

* Corresponding authors at: School of Physics and Electronic Engineering, Shanxi University, Taiyuan 030006, China.
E-mail addresses: sundd@sxu.edu.cn (D. Sun), mj@sxu.edu.cn (J. Ma).

https://doi.org/10.1016/j.optlastec.2024.111281
Received 20 March 2024; Received in revised form 10 May 2024; Accepted 4 June 2024
Available online 8 June 2024
0030-3992/

designed a curvature sensor consisting of a cascade of two cascaded tilted long period fiber gratings at opposite angles [22]. The sensor has a small detection range, which is not packaged and protected. 2019 Jingjing Guo et al. proposed a strain sensor with fiber Bragg grating (FBG) embedded in polydimethylsiloxane (PDMS) substrate for human activity detection. For highly wearable strain sensing [18]. The study does not indicate bend detection range sensitivity, and take no account of temperature cross sensitivity. 2021 Linqing Li et al. designed FBG embedded in silicone tubes, which is integrated into a finger protection strap and worn on a mechanical finger device for finger joint flexion monitoring [14]. The sensor is difficult to make, has low sensitivity, and does not studied the cross sensitivity of temperature. 2022 Weijiang Xu et al. demonstrated a upconversion luminescence based soft transparent fiber optic sensor that can detect temperature and curvature simultaneously with good linearity and repeatability sensing [24]. The study does not explain the curvature sensitivity, and the bending and detection range are small, which is not suitable for identifying bending direction. 2023 Yukun Shu et al. proposed a highly sensitive three-parameter (temperature, strain and bending) simultaneous measurement of thin-core fiber based-Mach-Zehnder interferometer(Shu et al., 2023). The sensor has low bending sensitivity and can not identify the direction, which is very easy to damage if not packaged. 2023 Xu Yue et al. proposed a wearable optical sensor based on an ultramicro FBG wrapped by a PDMS film. By combining an ultramicro optical fiber with an FBG, an ultramicro optical fiber Bragg grating for measuring various physical parameters, such as bending angle and temperature [25]. Although the sensor has a high sensitivity, the detection range is small and there is no package protection. 2023 Hao Li et al. proposed and confirmed a highly sensitive gas pressure sensor based on a fiber Mach-Zehnder interferometer, which uses PDMS and metalorganic frameworks mixture as gas-sensitive material(Li et al., 2023a). The study indicates that PDMS is a flexible material with high elasticity, which is suitable for human wearable devices, and the sensitivity of the sensor is significantly improved by adding a metal–organic framework to the PDMS. These exploratory works provide methodological references for the detection of wearable sensors, but these sensors often suffer from limitations such as difficult fabrication and low sensitivity. However, it gives us a new idea that doping different materials in PDMS can effectively improving the sensing performance, and molybdenum sulfide (MoS_2) has various excellent optical properties, such as large surface area and volume ratio, strong light absorption, and high mobility(Li et al., 2023b), which just gives us an option, and optical microfibers are characterized by low transmission loss, high mechanical strength, and high sensitivity [26,27]. These properties provide another technological platform for the application in wearable technology.

This paper describes a flexible wearable sensor that identifies bending direction and body temperature by wrapping a microfiber optic in a double layer of different membranes. In order to better put the microfiber into wearable sensor applications, PDMS, which is a highly flexible and biocompatible polymer with low refractive index, can be well used to encapsulate the microfiber as a way of avoiding the effects caused by environmental perturbations and damage to the fiber optic device. PDMS blended MoS_2 in appropriate amounts can effectively improve the sensitivity and bending direction recognition ability of the sensor.The sensor has different sensitivities for reverse bending and obverse bending response of 23.62 nm/m^{-1} and 2.70 nm/m^{-1}, respectively. The temperature sensitivity is 1.10 nm/°C for the range of 35 to 42 °C. Based on these sensitivities, a sensitivity matrix can be built and can be solved to achieve simultaneous temperature and bending measurements. The sensors have a fast response and high sensitivity, and can be applied to wrist injury and treatment monitoring and human body temperature monitoring. By varying the content of MoS_2 and the size of the film it is possible to obtain sensors with different characteristics for different usage scenarios. The simple structure and functionality of the sensor creates the possibility of developing a new type of flexible wearable sensor.

2. Experimental section

2.1. Regents and instruments

Monolayer molybdenum disulphide dispersion (1.0 mg/ml), and SYLGARD 184 SILICONE ELASTOMER (Polydimethylsiloxane PDMS) are purchased from Macklin Biochemistry Co., Ltd (Shanghai, China). The macroscopic structure of the microfibre interferometer is observed using an optical microscope (Caikon DMM-200C). Use a magnetic stirrer (MS-280-H) to prepare the reagents needed for the experiment.

The instruments used are an amplified spontaneous emission source (ASE, range 1528–1603 nm, power 10 dBm), a optical spectral analyser (OSA, AnritsuMS9740A, range 600–1700 nm), a fusion splicer (Fujimura 87S +), an electric shift table controller (ZOLIX MC600), a bending device(ZOLIX PA100), and a column temperature chamber (HT-330) etc.

2.2. Experimental setup

Fig. 1 (a) shows the experimental setup for bending measurement. Light is emitted from an ASE source, transmitted to a wearable sensor based on microfiber interferometer, and then detected by an OSA with a wavelength resolution of 0.03 nm. The microfiber interferometer is fabricated through a commercial optical (GF3) fiber by heating with a hydrogen flame and stretching with a taper puller (ZOLIX PA100, ZOLIX MC600). To avoid errors, the operation parameters of a taper puller are set, which include the speed of each taper pull of 2 mm/s, the acceleration of 5 mm/s^2, the maximum speed of 9 mm/s, and the taper pulling distance of 16 mm. A microfiber interferometer with good stability is successfully prepared, which is then encapsulated by PDMS materials. Fig. 1 (a, bottom) is the bending device for the calibration of bending experiment.

Fig. 1 (b) shows the schematic structure of the wearable sensor based on microfiber interferometer, where the light enters the microfiber interferometer encapsulated by a double-layer membrane shown in the figure from the left side and finally outputs from its right side. Fig. 1 (c) shows the corresponding structure parameters of the internal microfiber of Fig. 1 (b), including two transition regions with a length of about 2 mm and a homogeneous region with a waist length of 12 mm and a diameter of about 14 μm. These insets in the bottom right of Fig. 1 (c) are real pictures (homogeneous region and two transition regions) of the microfiber interferometer drawn by an optical microscope. The left inset of Fig. 1 (c) shows the transverse electric field amplitude distribution of HE_{11} and HE_{12} for the main interference modes.

2.3. Sensor fabrication

A total of five steps are needed to prepare the microfiber interferometer based wearable sensor, as shown in Fig. 1 (d). In the first step, the prepared PDMS solution is applied to the slide in a 4 cm long by 1.5 cm wide pattern, and heated by a heating stage at 80 °C for 20 min to obtain the PDMS film with a thickness of about 200 μm. Then, the PDMS film is detached from the slide by a razor blade, as shown in the right of Step 1, and the corresponding real figure is shown in the top of Fig. 1 (e). In the second step, prepare and fabricate the microfiber interferometer, which has been described in detail in Section 2.2, and the corresponding interference spectrum is shown in the right of Step 2. In the third step, straighten and place the microfiber interferometer in the middle of the PDMS, which fixed with tape at both ends, which has the corresponding to the interference spectrum in the right of Step 3. In the fourth step, the prepared mixed solution of PDMS and MoS_2 is dropped and coated uniformly on the aforementioned sample, and the corresponding interference spectrum is shown in the right of Step 4. In the fifth step, the sample obtained above is heated with a heating stage at 80 °C for 20 min to obtain a wearable sensor with a thickness of about 700 μm, and the corresponding interference spectrum after cooling is shown in the right

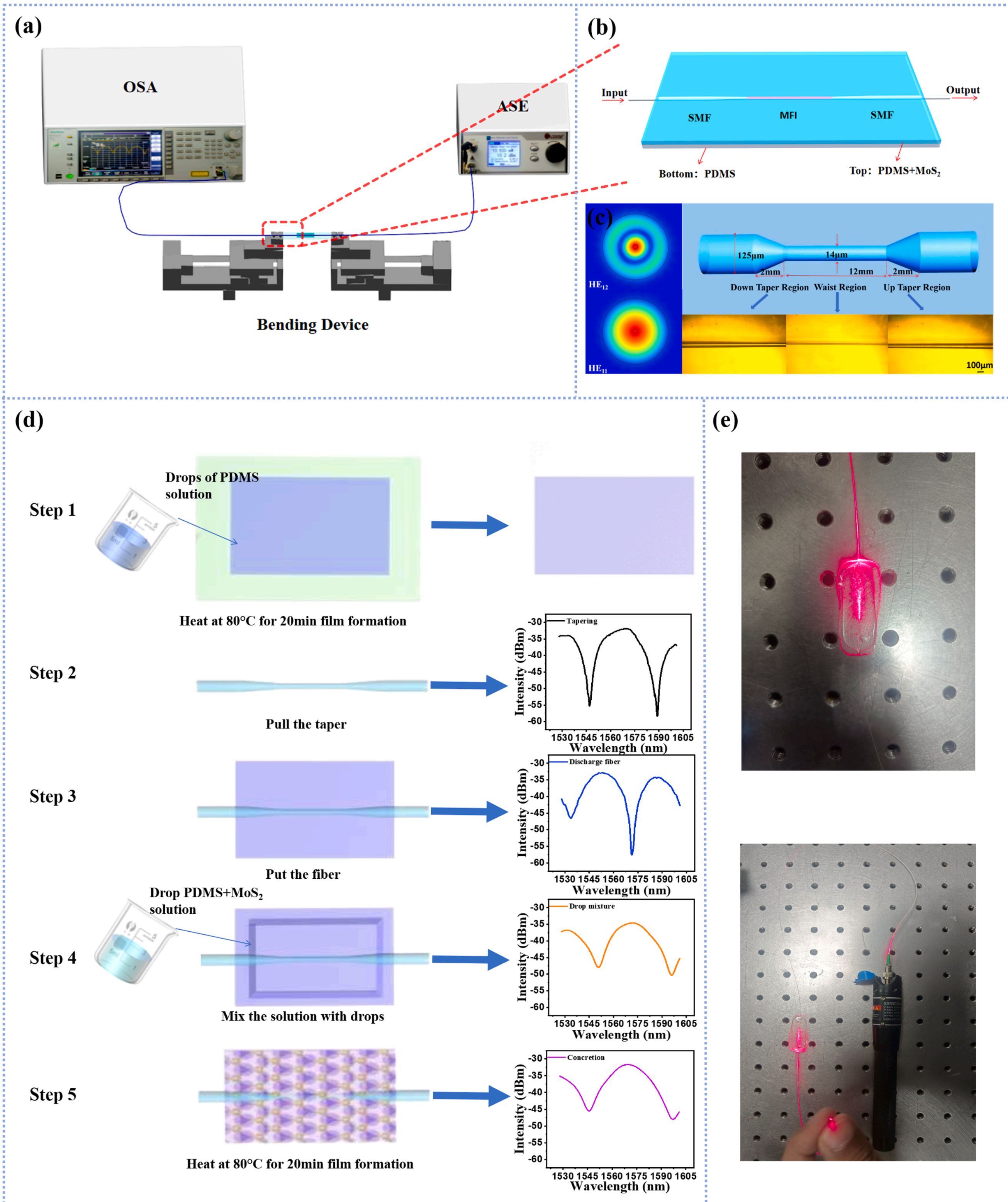

Fig. 1. **(a)** Diagram of the experimental set-up for measuring bending. **(b)** Structure of a wearable sensor based on microfiber interferometer. **(c)** Corresponding structure parameters of the microfiber interferometer, with transverse electric field amplitude distributions for the main interferometric modes HE_{11} and HE_{12} and real pictures by the optical microscope. **(d)** The fabrication process of microfiber interferometer-based wearable sensor and its corresponding interference spectrum. **(e)** The red light test procedure after this sensor is manufactured.

of Step 5, which has the red light test figure in the bottom of Fig. 1 (e).

2.4. Preparation of solution

Preparation of PDMS sol: Use a dropper to add the elastic polymer (Sylgard 184A) and the curing agent (Sylgard 184B). in the ratio of 10:1 into the beaker, and stir the above solution with a glass rod for 5 min to seal and stand for half an hour in order to eliminate the air bubbles, and then finally PDMS sol is obtained. The ratio of 10:1 is chosen because too large a ratio will make the film too hard and too soft, affecting the amount of sensor tensile bending, and too small a ratio will lead to the film is difficult to have enough flexibility.

Preparation of PDMS and MoS_2 mixed solution: the prepared PDMS sol and the monolayer MoS_2 dispersion (1.0 mg/ml) are selected to be added into the beaker in the ratios of 24:1, 12:1, 10:1, 8:1 and 4:1 with a dropper, which stirred for 5 mins with a glass rod, and left for half an hour after sealing to eliminate air bubbles. Finally the mixed solutions in different ratios are obtained.

3. Results and discussion

3.1. Sensing principle

Due to the thinning of the fiber diameter in the middle region of the microfiber, both the core and cladding diameters are reduced, resulting in a mismatch. Thus when incident light enters the microfiber, a portion of the light can continue to propagate along the core, and an another portion enters the tapered transition region of the microfiber, which excites the higher-order modes. The core and cladding modes are transmitted simultaneously with the predominantly propagating fundamental (HE_{11}) and higher order modes (HE_{12}), which are coupled at the other end of the tapered transition region. Due to the different transmission coefficients of the fundamental and higher order modes, interference fringes are formed when can met the interference conditions. The total interference intensity is expressed as:

$$I_T = I_{co} + I_{cl} + 2\sqrt{I_{co}I_{cl}}cos(\Delta\phi) \quad (1)$$

where I_{co} and I_{cl} are the intensities of the higher-order modes of the fundamental mode HE_{11} and HE_{12}, respectively. ϕ is the phase difference between the two interfering modes. L is the length of the girdle region. And the refractive index difference between the two modes is $\Delta n = n_{eff1} - n_{eff2}$[29], therefore, the phase difference between the two interference modes can be expressed as:

$$\phi = \frac{2\pi}{\lambda}\Delta nL \quad (2)$$

where λ is the centre wavelength of the incident light wave. ΔnL is the optical range difference between the two modes. Therefore, changes in the external environment will affect the refractive index difference between the two modes, which ϕ in turn will change and the interference wavelength will drift.

Bending the coupling coefficients and differentiating the wavelength's, we can get

$$\delta\phi = \frac{2\pi}{\lambda^2}L\left[\lambda\left(\frac{\partial\Delta n}{\partial C}\right)\bullet\delta C - \Gamma\bullet\delta\lambda\right] \quad (3)$$

$\Gamma = 1 - \frac{\lambda}{\Delta n}\frac{d\Delta n}{d\lambda}$ is the dispersion factor and δC is the bending rate of change [28]. Since the analysis yields $\frac{\partial\Delta n}{\partial C} > 0$ and $\Gamma < 0$ (HE_{11} group velocity is larger than that of HE_{12}), if it is to be made to be $\delta C > 0$, therefore at that time $\delta\lambda < 0$. Thus it can be obtained that when the interferometric microfiber device is bent, there is a blue-shift in the interferometric wavelength.

When the refractive index of the external environment changes very slowly, $\delta\phi = 0$. By calculation we can get

$$S = \frac{d\lambda}{dn_{MoS_2+C}} = \frac{\lambda}{\Gamma}\frac{\partial\Delta n}{\partial n_{MoS_2+C}} \quad (4)$$

where $\frac{\partial\Delta n}{\partial n_{MoS_2+C}}$ is the change in refractive index induced by the external environment [30,31]. That is, when the concentration of MoS_2 in the PDMS increases and changes in curvature, n_{MoS_2+C} increases, usually HE_{12} has a larger increment than the effective refractive index of HE_{11}, and hence $\frac{\partial\Delta n}{\partial n_{MoS_2+C}} < 0$. At the same time, $\Gamma < 0$, thus obtaining S as a positive number, which in turn yields a red-shift of the wavelength as the refractive index of the external environment increases.

Here the length of the waist region of the microfiber is taken as 90 μm, and the length of the transition is 15 μm, and the curved microfiber is simulated with the Rsoft software to obtain the energy distribution and mode field distribution of the X-Z cross-section light at curvatures of 4.31 m^{-1} and 6.43 m^{-1}. Comparing Fig. 2 (a, left) and Fig. 2 (b, left), it can be seen that as the curvature becomes larger, the light energy at the exit end of the microfiber becomes smaller and smaller in the energy distribution and the energy loss at the periphery of the fiber becomes larger. Comparing Fig. 2 (a, right) and Fig. 2 (b, right), it can be seen that in the mode field distribution, as the curvature becomes larger, the bends are getting bigger and the light transmission distance is getting smaller, and it can be clearly seen that when the curvature is too large, the mode field of the cone region at the end of the cone area starts to become smaller and there are a lot of burrs. Therefore, we can conclude that: As the bending curvature increases, the evanescent field of the microfiber is enhanced, but it increases the transmission loss, It means that these exists a balance between the sensitivity/ response time and transmission loss. Therefore no increasing blindly the curvature, the curvature is too large may lead to the light is locked in the transition, making it impossible to output light.

The parametric conversion between the moving distance and curvature of the fiber optic bending sensing structure is shown in Fig. 2 (c). Let the starting distance between the fixed end and the moving end be L_o, and the moving end be moved inward d, then the distance after the platform is moved becomes L_o-d. The conversion formula of the curvature (C) and the moving distance is expressed as follows:

$$C = \frac{1}{R} \approx \sqrt{\frac{24d}{L_0^3}} \quad (5)$$

when the phase difference $\phi = (2m+1)\pi$, the Mach-Zehnder interference condition is satisfied, which can be expressed by introducing it into Eq. 2 thereby obtaining the peak resonance wavelength (corresponding to the trough) of the transmission spectrum as:

$$\lambda_m = \frac{2\Delta n_{eff}L}{2m+1} \quad (6)$$

where λ_m denotes the wavelength of the m-order resonance peak. A change in the effective refractive index difference Δn_{eff} causes a displacement of the wavelength λ_m. Differentiating this resonance peak wavelength with respect to temperature yields the sensitivity with respect to temperature expressed as:

$$S_T = \frac{d\lambda_m}{dT} = \lambda_m\left(\frac{dL}{LdT} + \frac{d\Delta n_{eff}}{\Delta n_{eff}dT}\right) \quad (7)$$

here $\frac{dL}{LdT}$ is the thermal expansion coefficient (TEC) of the optical fiber The length L of the girdle region is almost constant, so the $\frac{dL}{LdT} = 0$, and $\frac{d\Delta n_{eff}}{\Delta n_{eff}dT}$ is the thermo-optical coefficient. When the temperature increases, due to the thermo-optical and thermal expansion effects of the optical fiber PDMS and molybdenum disulphide, here the thermal expansion coefficient $\alpha = 9.6 \times 10^{-4}$ /°C for PDMS, and the thermo-optical coefficient of -4.5×10^{-4} /°C for PDMS. Because of the high negative thermo-optic coefficient of PDMS, the resonant wavelength of this

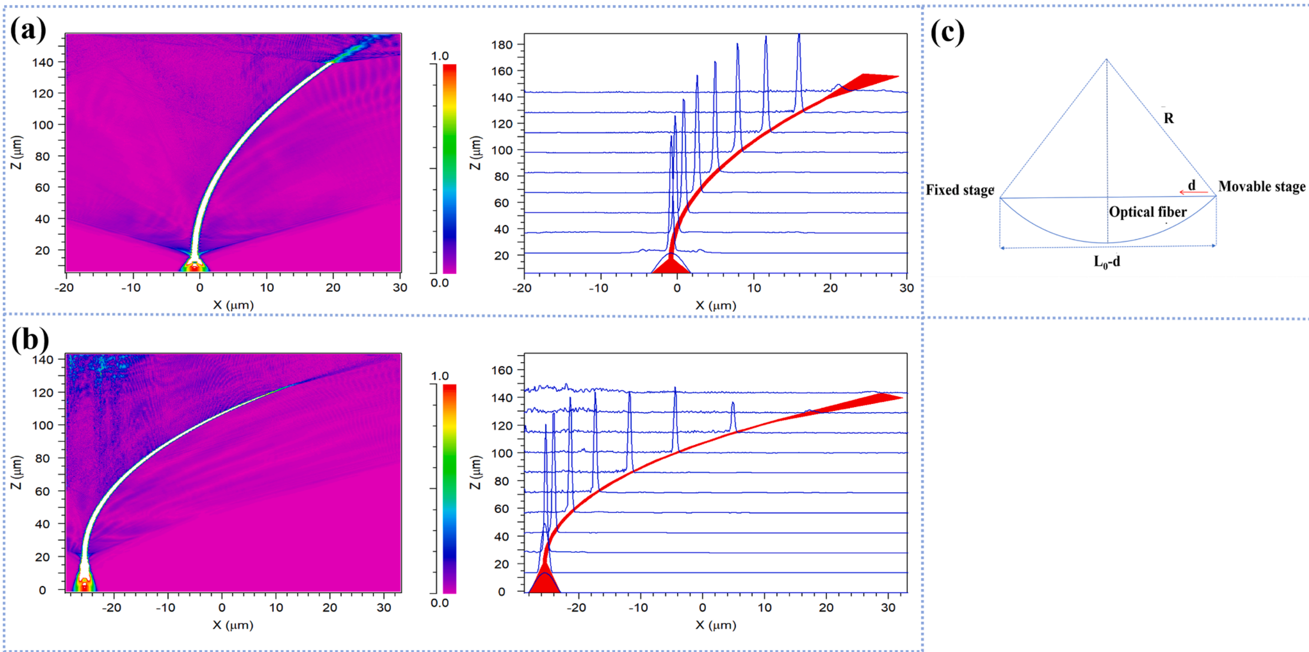

Fig. 2. Energy distribution and mode field distribution of X-Z cross-section light at curvatures of **(a)** 4.31 m^{-1} **(b)** 6.43 m^{-1}. **(c)** Bending principle diagram of simply supported beam structure.

sensor is red-shifted at elevated temperatures.

3.2. Bending performance test

3.2.1. Analysing the effect of different MoS_2 concentrations on reversed bending sensing

The experimental trial process obtains this wearable sensor is unstable in curvature of 0 m^{-1}-1 m^{-1}, so curvature measuring range measured starts from 1 m^{-1} to 6.5 m^{-1}, which sets every 0.25 m^{-1} from 1 m^{-1}-2 m^{-1}, and every 0.5 m^{-1} from 2 m^{-1}-6.5 m^{-1}. Fig. 3 shows the wavelength response of the sensor to curvature for the structure. Specifically, in Fig. 3 (a) the wavelength drifts of 61 nm, 70 nm, and 126 nm correspond to only PDMS and PDMS:MoS_2 volume ratio of 24:1, and 12:1, respectively. In Fig. 3 (b), the wavelength drifts are 215 nm, 121 nm, and 6.5 nm corresponding to the PDMS:MoS_2 volume ratio of 10:1,8:1, and 4:1, respectively. After analyzing the data of different ratios, it can be seen that the wavelength drift shows a trend of increasing and then decreasing with the increase of MoS_2 concentration. The reason for this phenomenon mainly is that the addition of MoS_2 in PDMS can change the refractive index and absorption characteristics of the optical fiber. The high concentration of MoS_2 can change the propagation characteristics (attenuation or distortion) of the optical signal due to absorb or scatter resulting in a reduction in sensitivity. The low concentration of MoS_2 in PDMS cannot increase sensitivity effectively. It means that the addition of MoS_2 in PDMS exists a balance between the sensitivity and transmission loss of the wearable sensor in bending response. The case of the package ratio of 10:1 (PDMS:MoS_2) has the largest sensitivity of bending response in curvature from 2 m^{-1} to 6.43 m^{-1}.

3.2.2. Bending detection

Because the microfiber are coated with two layers of different

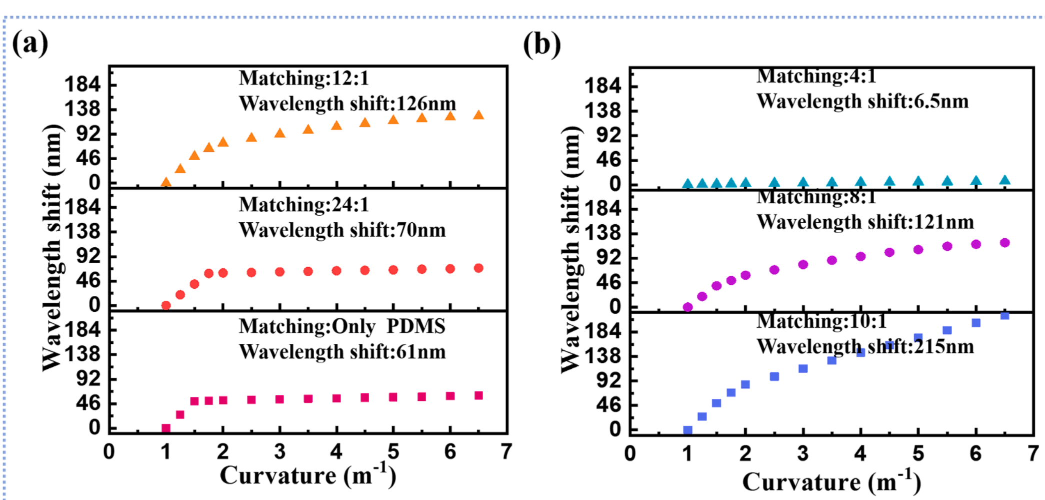

Fig. 3. Wavelength response of the wearable sensor at curvatures of 1 m^{-1}-6.43 m^{-1} **(a)** with only PDMS and PDMS:MoS_2 (24:1 and 12:1 v:v) **(b)** with PDMS:MoS_2 (10:1,8:1 and 4:1 v:v).

materials, the sensor has different sensitivities in the obverse and reverse directions. In order to demonstrate its usefulness, In this experiment is analysed here from curvature of 4.31 m^{-1} to 6.10 m^{-1}. Fig. 4 (a) analyses the interference spectrum in this curvature range for reverse bending, which corresponds to the right inset of Fig. 5 I (a). It can be seen that the interference spectrum of this interference spectrum is red-shifted, Wavelength shift is analysed linearly with a linearity of 0.98 and a sensitivity of 23.62 nm/m^{-1}. At a curvature of 4.31 m^{-1} to 4.98 m^{-1}, the intensity change can be seen from the interference spectrum, which is blue-shifted, and a linear analysis shows a sensitivity of 18.45 dBm/m^{-1} (a linearity of 0.98). At a curvature of 4.98 m^{-1} to 6.10 m^{-1}, a red-shift of the intensity change can be seen from the interference spectrum, which has a sensitivity of 12.68 dBm/m^{-1} (a linearity of 0.97). Fig. 4 (b) analyses the interference spectrum when the same curvature range is bent in the obverse direction, which corresponds to the left inset of Fig. 5 I (a), and it can be seen that the interference spectrum is blue-shifted, and a linear analysis has been performed with a linearity of 0.99 and a sensitivity of 2.70 nm/m^{-1}. At a curvature of 4.31 m^{-1} to 6.10 m^{-1}, it can be seen from the interference spectrum that the intensity change is red-shifted with a sensitivity of 3.60 dBm/m^{-1} (a linearity of 0.96). Based on Fig. 4 (a) and Fig. 4 (b) it can be concluded that the wavelengths of its reverse bending and obverse bending drift in different directions occurs, and there is a large difference in its sensitivity, which can accurately determine the direction of bending. As can be seen from Fig. 5 I (a), the sensor has good repeatability and a response time of 2 s and a recovery time of 2 s. Fig. 5 I (a) shows the real-time stabilised response of the system for the same amplitude bending. The results indicate that the wavelength changes are almost the same for 5 repetitions of reverse bending from 4.31 m^{-1} to 4.77 m^{-1} and obverse bending from 4.31 m^{-1} to 5.19 m^{-1}. Fig. 5 I (b) shows the real-time reproducible response of the system to different amplitude bending. The repeated experiments are performed for all sensors with curvatures of 4.31 m^{-1}, 4.55 m^{-1}, 4.77 m^{-1}, 4.98 m^{-1}, and 5.19 m^{-1}. The inset of Fig. 5 I (b) shows the corresponding bending real picture of the wrist during obverse bending. Fig. 5 I (c) shows the results after 33 repetitive bends from curvature of 4.31 to 4.77 m^{-1} for both obverse and reverse bends, from which it can be seen that the sensor has good repeatability. The test results show that the sensor has good stability and repeatability, and can have good recognition of reverse and obverse directions.

In this experiment, The wavelength response results of the sensor correspond to the four subjects are presented in Fig. 5 II. Each person will perform four measurement experiments in the bending of their wrists with the curvature from 4.31 to 5.93 m^{-1}.The centre of the sensor is attached to the position of the extensor support band of the wrist, and the position of the human ulnar styloid is fixed as initial value, then is rotated from 30° to 60° by a protractor. The data of the experiment is recorded once for every 5°, and the difference of the wavelength each time is made with that of the previous wavelength. The difference between the angle and curvature is transformed to obtain the curvature of Fig. 5 II. As can be seen in Fig. 5 II, the wavelength change in forward bending for every 5° change in angle is about 10 nm, and the wavelength change in reverse bending is about 1 nm, and the overall trend is still in line with the law of Fig. 5 I. Due to the high sensitivity of reverse bending, each person bending the same angle corresponding to the curvature of the larger differences in the measured data also have relatively large differences, but reverse bending due to its relatively low sensitivity, by the outside world is not very large, the data is more stable. The sensor has fast response speed and high sensitivity, and can accurately distinguish the bending direction. It can be applied to wrist injury and treatment monitoring.

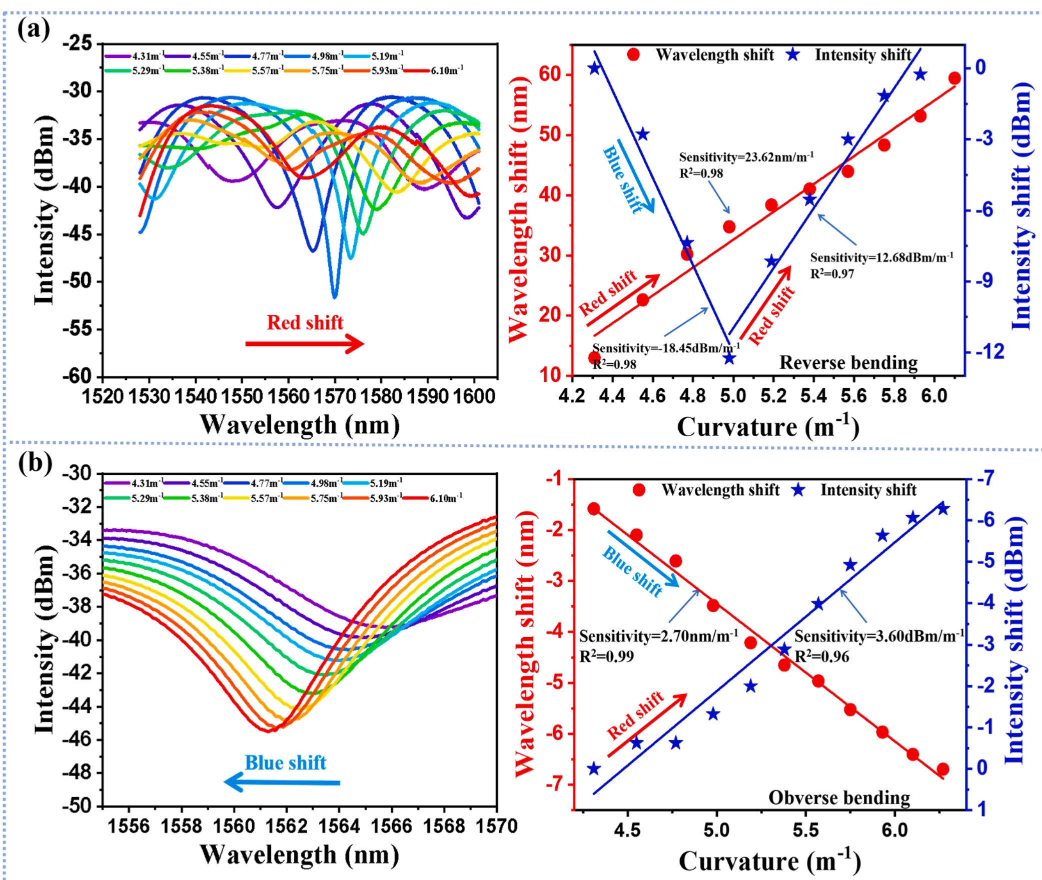

Fig. 4. **(a)** Interference spectrum and linear analysis of the structure bent in the reverse direction (the right inset of Fig. 5 I (a)) with different curvatures. **(b)** Interference spectrum and linear analysis of the structure bent in the obverse direction (the left inset of Fig. 5 I (a)) with different curvatures.

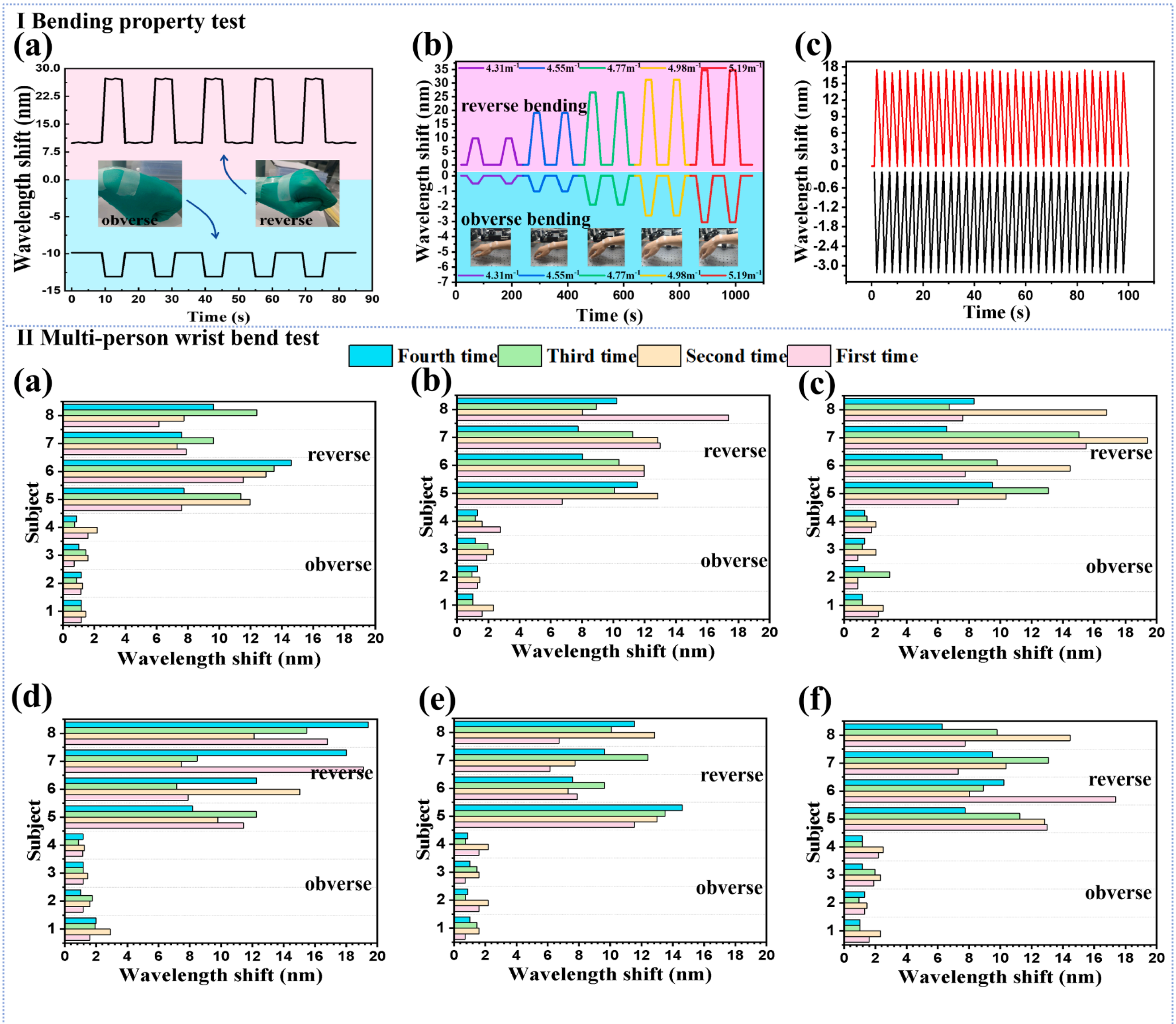

Fig. 5. **I Bending property test (a)** Real time stable response of the system to the same amplitude bending. **(b)** Real time repeatable response of the system to different amplitude bends. **(c)** 33 repetitions of obverse and reverse bending **II Multi-person wrist bend test** Bar graph of wavelength displacements of six bending curvatures measured by the sensor (four subjects) **(a)** 4.31 m^{-1} **(b)** 4.55 m^{-1} **(c)** 4.98 m^{-1} **(d)** 5.29 m^{-1} **(e)** 5.57 m^{-1} **(f)** 5.93 m^{-1}.

3.3. Temperature monitoring

The experiment analyses the temperature change from 30 °C to 45 °C. Fig. 6 (a) displays the interference spectrum of the sensor for this rising temperature range, which can be seen to be red-shifted, and a linearity analysis is carried out from 35 °C to 42 °C, with a sensitivity of 1.10 nm/°C in wavelength shift (a linearity of 0.99). The intensity of the interference spectrum is blue-shifted over the same range of temperature variations, and a linear analysis of the spectrum shows a linearity of 0.96 and a sensitivity of 0.40 dBm/°C. The inset on the right side of Fig. 6 (a) shows the results of repeated experiments with the sensor at rising temperatures. The standard deviation of the wavelength drift for each temperature is calculated and averaged to obtain the average sensitivity of the three experiments. Fig. 6 (b) shows the interference spectrum of the sensor for this temperature range of cooling, which can be seen to be blue-shifted, and a linearity analysis is carried out from 35 °C to 42 °C, with a linearity of 0.99 and a sensitivity of 0.98 nm/°C. The inset on the right side of Fig. 6 (b) shows the results of repeated experiments with the sensor cooled down. The standard deviation of wavelength drift for each temperature is calculated and averaged to obtain a average sensitivity. The above experimental results confirm the good reproducibility of the sensor and show that the sensor is stable during heating and cooling.

Fig. 7 (a) depicts the real-time wavelength shift with temperature change during each step. The time required for the wavelength shift to stabilize is 140 s for each 1 °C change in temperature from 37 °C to 42 °C. The repeatability of the system response is tested by a cooling change in temperature, and the time required for the wavelength shift to stabilize is 200 s, which is comparable to a commercially available mercury temperature monitoring device. As shown in the inset of Fig. 7 (a), the sensor is applied to on the forehead of the volunteer to monitor the body temperature in real-time. The sensor reflects the change of body temperature from 37 °C to 42 °C. Fig. 7 (b) shows the recording of wavelength over time to test the stability of this sensor. In total, 35 °C, 38 °C, and 41 °C are tested for wavelength changes over 6 min, and the repeated experiments have completed to calculate the standard deviation of the wavelength drift at the same temperature for obtaining the error range. Fig. 7 (c) shows the results after 30 repetitive temperature from curvature of 37 °C to 38 °C for temperature, from which it can be

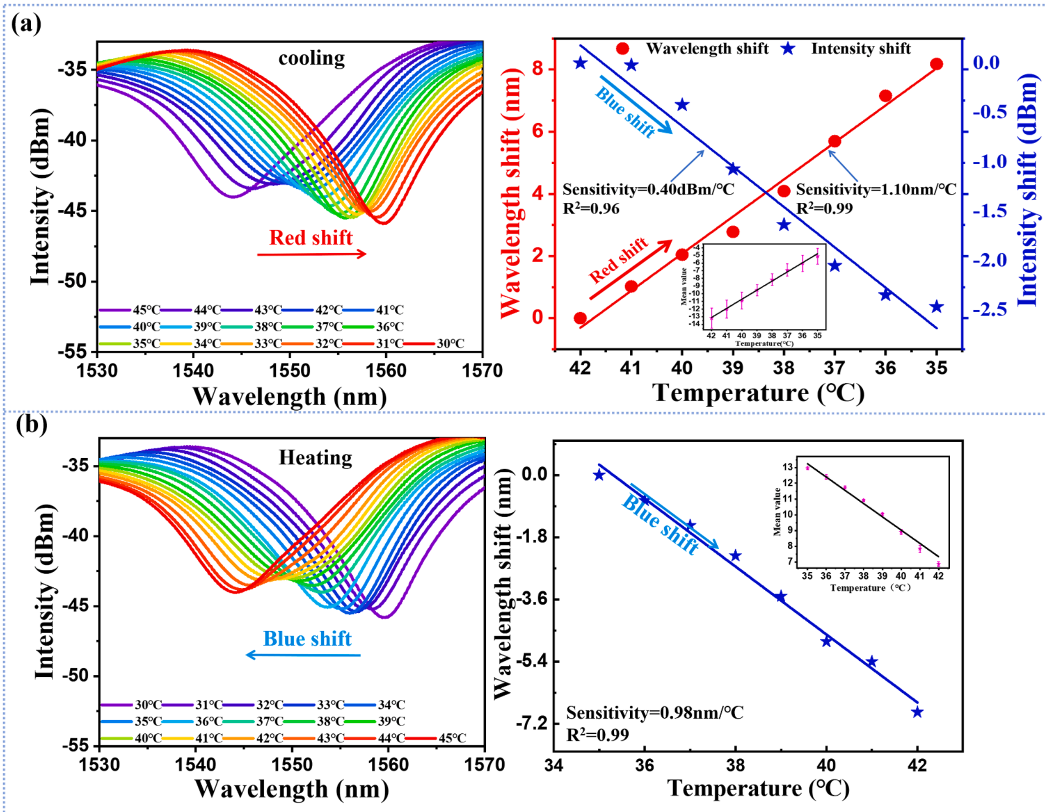

Fig. 6. **(a)** Interference spectrum and linear analysis of the sensor at rising temperatures. **(b)** Interference spectrum and linear analysis of the sensor at falling temperatures.

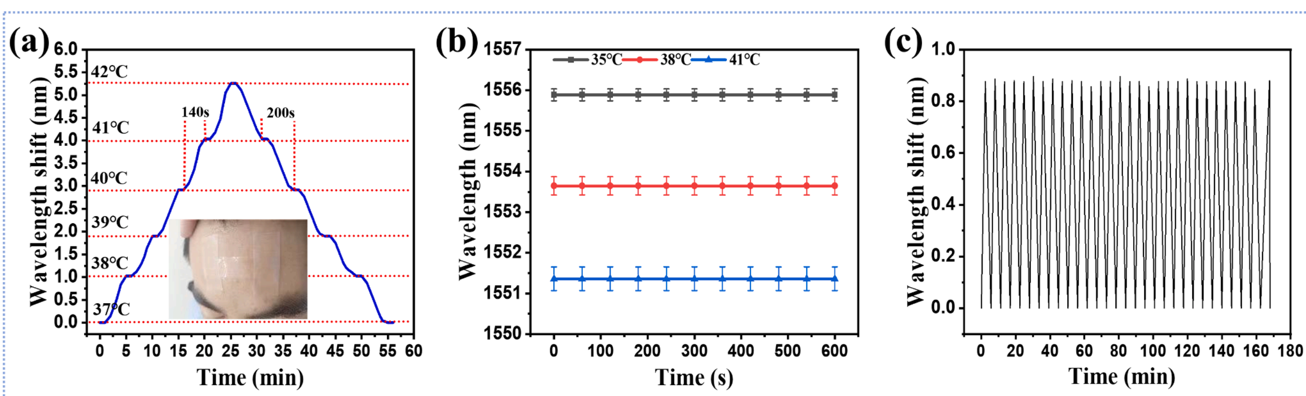

Fig. 7. **(a)** Real-time repetitive response of the system to different temperature changes. **(b)** Real-time stable response of the system to the same temperature. **(c)** 30 repetitions of temperature.

seen that the sensor has good repeatability. Therefore, From Fig. 7 (a), Fig. 7 (b) and Fig. 7 (c), it can be seen that the sensor is able to detect the magnitude of temperature change with a faster response, repeatability and stability. Thus the proposed sensor can promote its wide application in temperature monitoring.

Table 1 shows the different structures of sensors for detecting bending temperature. In contrast, our sensor has high sensitivity, low cost, easy to make and identify the direction of bending, which is encapsulated to reduce the interference of external factors.

3.4. Bending and temperature two-parameter analysis

For optical fiber sensors, the study of temperature cross sensitivity is very important, which jointly affects the change of transmission spectrum wavelength and reduces the detection accuracy of the sensor. Thus, the actual test results must be compensated and adjusted accordingly. Assume the influence of n external parameters of the optical fiber sensor, that is:

$$\Delta X = \begin{bmatrix} \Delta X_1 \\ \vdots \\ \Delta X_n \end{bmatrix} \tag{8}$$

where $\Delta X_i(i = 1\cdots n)$ represents each physical parameter. ΔY is the variation of optical parameters, such as intensity, wavelength, frequency, etc., obtained from measurements, and the relationship between the variation of the optical parameters inside the sensor, ΔY, and

Table 1
Comparison of Curvature and Temperature detection methods.

Structure	Curvature sensitivity	Curvature range	Temperature sensitivity	Cost	Encapsulation or not	Bending direction or not	Year	Ref.
Two cascaded 6°tilted long period fiber gratings	-15.4935 nm/m^{-1} 15.2852 nm/m^{-1}	0.5 to 2 m^{-1}	0.0406 nm/°C	Low	No	Yes	2017	[22]
Fiber Bragg grating	No	No	No	Medinm	Yes	Yes	2019	[18]
Fiber Bragg grating	5.6 ± 0.5 pm/°.	0 to 80°	No	High	Yes	Yes	2021	[14]
Upconversion luminescence	No	0.192 to 0.213 mm^{-1}	714.82 K^{-1}	High	Yes	No	2022	[24]
Microfiber Bragg grating	0.19 nm/°	0° to 90∘.	0.04 nm/°C	Medinm	Yes	No	2023	[36]
Single-mode-no-core –thin-core-single-mode fiber	-24.784 nm/m^{-1}	0.6847 to 1.1354 m^{-1}	248.7 pm/°C	Low	No	No	2023	[25]
Microfiber interferometer	23.62 nm/m^{-1} 2.70 nm/m^{-1}	1 to 6.43 m^{-1}	1.10 nm/°C	Low	Yes	Yes	This work	This work

each external parameter is established in the form of a matrix:

$$\Delta Y=\begin{bmatrix}\Delta y_1\\ \vdots\\ \Delta y_n\end{bmatrix}=\begin{bmatrix}k_{x_{1,1}} & \cdots & k_{x_{n,1}}\\ \vdots & \ddots & \vdots\\ k_{x_{1,n}} & \cdots & k_{x_{n,n}}\end{bmatrix}\begin{bmatrix}\Delta x_1\\ \vdots\\ \Delta x_n\end{bmatrix} \tag{9}$$

The inverse of K is calculated to obtain the measured external parameters as [32]:

$$\Delta X=K^{-1}\Delta Y=\frac{K^*}{|K|}\Delta Y \tag{10}$$

Based on the above experimental bending and temperature response results, it can be found that the wavelength and extinction ratio offsets ($\Delta\lambda$ and Δt) are linear with respect to C (curvature) and T (temperature), and a sensor matrix for simultaneous measurement of C and T can be established, denoted as [33]:

$$\begin{bmatrix}\Delta\lambda\\ \Delta t\end{bmatrix}=\begin{bmatrix}K_{\lambda,C} & K_{\lambda,T}\\ K_{t,C} & K_{t,T}\end{bmatrix}\begin{bmatrix}\Delta C\\ \Delta T\end{bmatrix} \tag{11}$$

where $\Delta\lambda$ and Δt are the wavelength shift and extinction ratio change of the inclination [15,34,35]. The ratio of the matrices $K_{\lambda,C}/K_{t,C}$ is not similar to $K_{\lambda,T}/K_{t,T}$, indicating that the matrices can be used to resolve the effects of C and T from wavelength and transmitted intensity, enabling simultaneous measurements of C and T. Two parameters of ΔC and ΔT (changes in relative bending and temperature) can be calculated from the cross matrix as:

$$\begin{bmatrix}\Delta C\\ \Delta T\end{bmatrix}=\begin{bmatrix}K_{\lambda,C} & K_{\lambda,T}\\ K_{t,C} & K_{t,T}\end{bmatrix}^{-1}\begin{bmatrix}\Delta\lambda\\ \Delta T\end{bmatrix}=\frac{1}{K_{\lambda,C}K_{t,T}-K_{\lambda,T}K_{t,C}}\begin{bmatrix}K_{t,T} & -K_{\lambda,T}\\ -K_{t,C} & K_{\lambda,C}\end{bmatrix}\begin{bmatrix}\Delta\lambda\\ \Delta t\end{bmatrix} \tag{12}$$

When detecting reverse bending in the curvature range of 4.31 m^{-1} to 4.98 m^{-1}, the test data of $K_{\lambda1,C}=23.62\,\text{nm/m}^{-1}$ and $K_{t1,C}=18.45\,\text{dBm/m}^{-1}$ can be known from the right panel of Fig. 4 (a). The test data of $K_{\lambda1,T}=1.10\,\text{nm}/^{\circ}\text{C}$ and $K_{t1,T}=0.40\,\text{dBm}/^{\circ}\text{C}$ for temperature can be known from the right panel of Fig. 6 (a). The above values are taken into the matrix (12). The final analytical expression of the matrix is given by:

$$\begin{bmatrix}\Delta C\\ \Delta T\end{bmatrix}=\frac{1}{-10.847}\begin{bmatrix}0.40 & -1.10\\ -18.45 & 1.10\end{bmatrix}\begin{bmatrix}\Delta\lambda 1\\ \Delta t1\end{bmatrix} \tag{13}$$

Because the ratio of the matrix $K_{\lambda1,C}/K_{t1,C}$ is not similar to the ratio of $K_{\lambda1,T}/K_{t1,T}$, it can analyze the influence of C and T on the trough from the wavelength and transmission intensity for realizing the simultaneous measurement.

When detecting reverse bending in the curvature range of 4.98 m^{-1} to 6.10 m^{-1}, the date of $K_{\lambda2,C}=23.62nm/m^{-1}$ and $K_{t2,C}=12.68dBm/m^{-1}$ are obtained from the right panel of Fig. 4 (a). The test data of $K_{\lambda2,T}=1.10\,\text{nm}/^{\circ}\text{C}$ and $K_{t2,T}=0.40\,\text{dBm}/^{\circ}\text{C}$ for temperature can be known from the right panel of Fig. 6 (a). The above values are taken into the matrix (12). The final analytical expression of the matrix is given by:

$$\begin{bmatrix}\Delta C\\ \Delta T\end{bmatrix}=\frac{1}{-4.5}\begin{bmatrix}0.40 & -1.10\\ -12.68 & 23.62\end{bmatrix}\begin{bmatrix}\Delta\lambda 2\\ \Delta t2\end{bmatrix} \tag{14}$$

By the same token, the simultaneous measurement of C and T can be achieved.

When detecting obverse bending in the curvature range of 4.31 m^{-1} to 6.10 m^{-1}, the date of $K_{\lambda3,C}=23.62\,\text{nm/m}^{-1}$ and $K_{t3,C}=3.60\,\text{dBm/m}^{-1}$ are obtained from the right panel of Fig. 4 (b). The test data of $K_{\lambda3,T}=1.10\,\text{nm}/^{\circ}\text{C}$ and $K_{t3,T}=0.40\,\text{dBm}/^{\circ}\text{C}$ for temperature can be known from the right panel of Fig. 6 (a). The above values are taken into the matrix (12). The final analytical expression of the matrix is given by:

$$\begin{bmatrix}\Delta C\\ \Delta T\end{bmatrix}=\frac{1}{-2.88}\begin{bmatrix}0.40 & -1.10\\ 3.60 & 2.70\end{bmatrix}\begin{bmatrix}\Delta\lambda 3\\ \Delta t3\end{bmatrix} \tag{15}$$

Similarly, the cross-sensitivity of C and T can be eliminated.

The above analysis shows that in the obverse bending and reverse bending, the matrix can be used to discriminate the effects of C and T for eliminating the temperature cross-sensitivity.

4. Conclusions

In this work, a flexible wearable optical microfiber sensor for identifying bending direction and body temperature is proposed. The sensor consists of a microfiber encapsulated with two layers of different membranes (MoS_2 and PDMS), which dopes different materials in PDMS can effectively improving the sensing performance. The results show that the sensor has a sensitivity response of 23.62 nm/m^{-1} in reverse bending and 2.70 nm/m^{-1} in obverse bending at a curvature range of 4.31 to 6.10 m^{-1}. The sensitivity is 1.10 nm/°C in the temperature range of 35 to 42 °C. A number of cyclic bending and temperature experiments, combined with standard deviation analysis, show that the sensor has good reproducibility and stability, which is tested on the left wrist of the individuals with different curvatures and on the forehead with body temperature. The sensor has high bending sensitivity, accurately identifies reverse and obverse bending, and detects body temperature quickly and accurately. At the same time, the sensitivity matrix is constructed by using wavelength and intensity demodulation methods to measure wrist bending and body temperature simultaneously. It is an optical option for future multiparameter monitoring and has a promising application in bio-health monitoring and rehabilitation training.

CRediT authorship contribution statement

Wenwen Wang: Writing – original draft, Methodology, Investigation, Formal analysis, Data curation. **Li Jin:** Investigation, Formal analysis, Data curation. **Guoxin Shi:** Methodology, Investigation, Formal analysis. **Ze Xu:** Methodology, Investigation, Formal analysis. **Yingkuan Guo:** Methodology, Investigation. **Bowen Yang:** Methodology, Investigation. **Yukun Yang:** Methodology, Funding acquisition.

Jizhou Wu: Project administration, Funding acquisition. **Dandan Sun:** Writing – review & editing, Methodology, Investigation, Funding acquisition, Formal analysis. **Jie Ma:** Resources, Project administration, Funding acquisition.

Declaration of competing interest

The authors declare that they have no known competing financial interests or personal relationships that could have appeared to influence the work reported in this paper.

Data availability

Data will be made available on request.

Acknowledgments

This work was supported by National Natural Science Foundation of China (62005147, U2341211, 32072301, 62175140, 62020106014).

References

[1] J. Tu, R.M. Torrente-rodriguez, M. Wang, et al., The era of digital health: a review of portable and wearable affinity biosensors, Adv. Funct. Mater. 30 (2019) 1906713, https://doi.org/10.1002/adfm.201906713.

[2] A. Nag, S.C. Mukhopadhyay, J. Kosel, Wearable flexible sensors: a review, IEEE Sens. J. 17 (2017) 3949–3960, https://doi.org/10.1109/jsen.2017.2705700.

[3] M. Amjadi, K.U. Kyung, I. Park, et al., Stretchable, skin-mountable, and wearable strain sensors and their potential applications: a review, Adv. Funct. Mater. 26 (2016) 1678–1698, https://doi.org/10.1002/adfm.201504755.

[4] S.Z. Homayounfar, T.I. Andrew, Wearable sensors for monitoring human motion: a review on mechanisms, materials, and challenges, SLAS Technol. 25 (2020) 9–24, https://doi.org/10.1177/2472630319891128.

[5] Y. Zhao, Z. Lin, S. Dong, et al., Review of wearable optical fiber sensors: drawing a blueprint for human health monitoring, Opt. Laser Technol. 161 (2023) 109227, https://doi.org/10.1016/j.optlastec.2023.109227.

[6] S. Bashardoust tajali, J.C. Macdermid, R. Grewal, et al., Reliability and validity of electro-goniometric range of motion measurements in patients with hand and wrist limitations, Open Orthop 10 (2016) 190–205, https://doi.org/10.2174/1874325001610010190.

[7] M. Rdest, D. Janas, Carbon nanotube wearable sensors for health diagnostics, Sensors (Basel) 21 (2021) 5847, https://doi.org/10.3390/s21175847.

[8] A. Rovera, A. Tancau, N. Boetti, et al., Fiber optic sensors for harsh and high radiation environments in aerospace applications, Sensors 23 (2023) 2512, https://doi.org/10.3390/s23052512.

[9] O. Atalay, A. Atalay, J. Gafford, et al., A highly sensitive capacitive-based soft pressure sensor based on a conductive fabric and a microporous dielectric layer, Adv. Mater. Technol. 3 (2017) 1700237, https://doi.org/10.1002/admt.201700237.

[10] M. Zhu, Q. Shi, T. He, et al., Self-powered and self-functional cotton sock using piezoelectric and triboelectric hybrid mechanism for healthcare and sports monitoring, ACS Nano 13 (2019) 1940–1952, https://doi.org/10.1021/acsnano.8b08329.

[11] C. Dong, A. Leber, T. Dasgupta, et al., High-efficiency super-elastic liquid metal based triboelectric fibers and textiles, Nat. Commun. 11 (2020) 3537, https://doi.org/10.1038/s41467-020-17345-8.

[12] D. Yang, Y. Liu, Y. Wang, et al., Integrated optic-fiber sensor based on enclosed efpi and structural phase-shift for discriminating measurement of temperature, pressure and RI, Opt. Laser Technol. 126 (2020) 106112, https://doi.org/10.1016/j.optlastec.2020.106112.

[13] W. Yuan, L. Li, Y. Wang, et al., Temperature and curvature insensitive all-fiber sensor used for human breath monitoring, Opt. Express 29 (2021) 26375–26384, https://doi.org/10.1364/OE.433959.

[14] L. Li, R. He, M.S. Soares, et al., Embedded FBG-based sensor for joint movement monitoring, IEEE Sens. J. 21 (2021) 26793–26798, https://doi.org/10.1109/jsen.2021.3120995.

[15] D. Xiao, G. Wang, F. Yu, et al., Optical curvature sensor with high resolution based on in-line fiber Mach-Zehnder interferometer and microwave photonic filter, Opt. Express 30 (2022) 5402–5413, https://doi.org/10.1364/OE.445982.

[16] Z. Wang, Z. Chen, L. Ma, et al., Optical microfiber intelligent sensor: wearable cardiorespiratory and behavior monitoring with a flexible wave-shaped polymer optical microfiber, ACS Appl. Mater. Interfaces 16 (2024) 8333–8345, https://doi.org/10.1021/acsami.3c16165.

[17] J.H. Li, J.H. Chen, F. Xu, Sensitive and wearable optical microfiber sensor for human health monitoring, Adv. Mater. Technol. 3 (2018) 1800296, https://doi.org/10.1002/admt.201800296.

[18] J. Guo, B. Zhou, R. Zong, et al., Stretchable and highly sensitive optical strain sensors for human-activity monitoring and healthcare, ACS Appl. Mater. Interfaces 11 (2019) 33589–33598, https://doi.org/10.1021/acsami.9b09815.

[19] Y. Cao, X. Wang, T. Guo, et al., High-resolution and temperature-compensational her2 antigen detection based on microwave photonic interrogation, Sens. Actuators B Chem. 245 (2017) 583–589, https://doi.org/10.1016/j.snb.2017.01.085.

[20] P. Xiao, Z. Xu, D. Hu, et al., Efficiently writing bragg grating in high-birefringence elliptical microfiber for label-free immunosensing with temperature compensation, Adv. Fiber Mater. 3 (2021) 321–330, https://doi.org/10.1007/s42765-021-00087-7.

[21] Y. Ran, Z. Xu, M. Chen, et al., Fiber-Optic Theranostics (FOT): interstitial fiber-optic needles for cancer sensing and therapy, Adv. Sci. 9 (2022) e2200456, https://doi.org/10.1002/advs.202200456.

[22] Y.P. Li, W.G. Zhang, S. Wang, et al., Bending vector sensor based on a pair of opposite tilted long-period fiber gratings, IEEE Photon. Technol. Lett. 29 (2017) 224–227, https://doi.org/10.1109/lpt.2016.2636446.

[23] J. Guo, K. Zhao, B. Zhou, et al., Wearable and skin-mountable fiber-optic strain sensors interrogated by a free-running, dual-comb fiber laser, Adv. Opt. Mater. 7 (2019) 1900086.1–1900086.9, https://doi.org/10.1002/adom.201900086.

[24] W. Xu, Y. Li, J. Shang, et al., Optical fiber sensor based on upconversion luminescence for synchronous temperature and curvature sensing, Opt. Express 30 (2022) 33136–33144, https://doi.org/10.1364/OE.464556.

[25] X. Yue, R. Lu, Q. Yang, et al., Flexible wearable optical sensor based on optical microfiber bragg grating, J. Lightwave Technol. 41 (2023) 1858–1864, https://doi.org/10.1109/jlt.2022.3227186.

[26] H.T. Zhu, L.W. Zhan, Q. Dai, et al., Self-assembled wavy optical microfiber for stretchable wearable sensor, Adv. Opt. Mater. 9 (2021) 2002206, https://doi.org/10.1002/adom.202002206.

[27] Y. Zhao, J. Liu, H. Li, et al., An ultra-sensitive gas pressure sensor based on tapered fiber coated with pdms film working at tap, Opt. Laser Technol. 151 (2022) 107998, https://doi.org/10.1016/j.optlastec.2022.107998.

[28] Y. Huang, Z. Tian, L.P. Sun, et al., High-sensitivity DNA biosensor based on optical fiber taper interferometer coated with conjugated polymer tentacle, Opt. Express 23 (2015) 26962–26968, https://doi.org/10.1364/OE.23.026962.

[29] P. Gong, X. Li, X. Zhou, et al., Optical fiber sensors for glucose concentration measurement: A review, Opt. Laser Technol. 139 (2021) 106981, https://doi.org/10.1016/j.optlastec.2021.106981.

[30] D. Sun, Y. Fu, Y. Yang, Label-free detection of breast cancer biomarker using silica microfiber interferometry, Opt. Commun. 463 (2020) 125375, https://doi.org/10.1016/j.optcom.2020.125375.

[31] L.P. Sun, J. Li, Y. Tan, et al., Bending effect on modal interference in a fiber taper and sensitivity enhancement for refractive index measurement, Opt. Express 21 (2013) 26714–26720, https://doi.org/10.1364/OE.21.026714.

[32] Y. Ma, S. Wang, X. Li, et al., Torsion and temperature sensor based on polished MSM structure, IEEE Photon. Technol. Lett. 32 (2020) 1117–1120, https://doi.org/10.1109/lpt.2020.3013855.

[33] W. Tao, L. Yang, J. Tang, et al., Simultaneous measurement of torsion and strain using a parallel structured fiber wave-guide sensor, Measurement 223 (2023) 113826, https://doi.org/10.1016/j.measurement.2023.113826.

[34] Y. Bai, Y. Miao, H. Zhang, et al., Simultaneous measurement of relative humidity and temperature using a microfiber coupler coated with molybdenum disulfide nanosheets, Opt. Mater. Express 9 (2019) 2846–2858, https://doi.org/10.1364/ome.9.002846.

[35] Y. Bai, Y. Miao, H. Zhang, et al., Simultaneous measurement of temperature and relative humidity based on a microfiber sagnac loop and MoS_2, J. Lightwave Technol. 38 (2020) 840–845, https://doi.org/10.1109/jlt.2019.2947644.

[36] Y. Shu, L. Li, J.W. Gao, et al., Simultaneous measurement three parameters of temperature, strain, and curvature by thin-core fiber based-Mach-Zehnder interferometer, Opt. Fiber Technol. 80 (2023) 103377, https://doi.org/10.1016/j.yofte.2023.103377.